

RESEARCH ARTICLE OPEN ACCESS

Bottom-Up Assembly of Amorphous Metal–Organic Frameworks From Proton Conductive Metal–Organic Polyhedra

 Nattapol Ma¹  | Daiki Umeyama² | Hiroki Yamada³ | Soracha Kosasang¹

¹International Center for Young Scientists (ICYS), National Institute for Materials Science, Tsukuba, Ibaraki, Japan | ²Research Center for Macromolecules and Biomaterials, National Institute for Materials Science (NIMS), Tsukuba, Ibaraki, Japan | ³Diffraction and Scattering Division, Japan Synchrotron Radiation Research Institute (JASRI), Sayo, Hyogo, Japan

Correspondence: Nattapol Ma (ma.nattapol@nims.go.jp)

Received: 4 March 2026 | **Revised:** 1 May 2026 | **Accepted:** 5 May 2026

Keywords: amorphous | coordination polymers | metal–organic frameworks | metal–organic polyhedra | proton conductivities

ABSTRACT

While crystalline metal–organic frameworks (MOFs) benefit from precise structural programmability, achieving comparable control in amorphous MOFs (aMOFs) remains underexplored. Most reported aMOFs are obtained via top-down amorphization of crystalline frameworks, whereas the limited bottom-up approaches typically rely on linker substitution-based assembly that inherently restricts node-level functionalization. Here, we present a bottom-up strategy for constructing proton-conductive aMOFs using sulfonate-rich metal–organic polyhedra (MOPs) as predesigned molecular building units. Discrete Rh-based MOPs with accessible axial coordination sites are crosslinked with flexible ditopic linkers to form extended amorphous networks while preserving intrinsic node functionality. Variation of linker identity modulates network connectivity, free volume, water stability, and proton transport behavior. Retention of the sulfonate group from the MOP building units affords aMOFs with proton conductivities of up to 4.8 mS cm^{−1} at 85°C and 90% relative humidity, with a low activation energy of 0.20 eV, whereas the sulfonate-free aMOF analog exhibits insulating behavior. These results establish a general strategy for the rational design of functionally programmable aMOFs using chemically predefined building units.

1 | Introduction

The precise spatial organization of molecular building blocks through coordination bonding underpins the development of metal–organic frameworks (MOFs) and porous coordination polymers (PCPs) [1–3]. This modular design strategy enables the rational assembly of extended architectures by linking inorganic nodes with organic linkers into predictable, long-range networks. While framework topology is dictated by the coordination geometry of the constituent units, the local chemical environment can be systematically tuned through the choice of metal centers and linker functionalities [4, 5]. The use of predetermined secondary

building units (SBUs), synthesized prior to framework formation, significantly expands the structural and chemical design space of MOFs and PCPs [6]. Such versatile structural and chemical control has established MOFs as a promising platform for a wide range of applications, including gas storage and separation [7–9], catalysis [10, 11], charge and ion transport [12–14], magnetism [15, 16], and more.

In contrast, extending comparable levels of structural programmability and functional control to the emerging class of amorphous MOFs (aMOFs) remains relatively underexplored [17]. The absence of long-range periodicity can impart

This is an open access article under the terms of the [Creative Commons Attribution-NonCommercial](https://creativecommons.org/licenses/by-nc/4.0/) License, which permits use, distribution and reproduction in any medium, provided the original work is properly cited and is not used for commercial purposes.

© 2026 The Author(s). *Small* published by Wiley-VCH GmbH

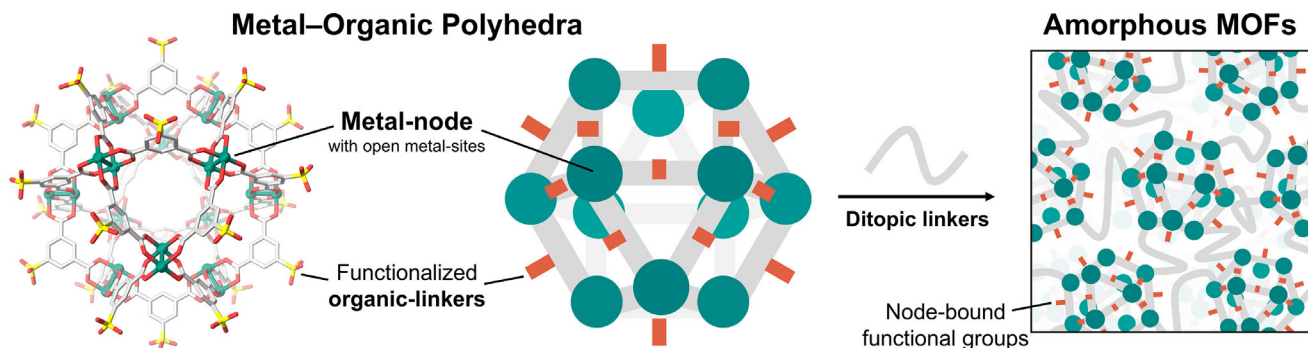


FIGURE 1 | Schematic representation of the bottom-up assembly of functionally programmable aMOFs. This modular approach utilizes Rh-based MOPs as chemically designable nodes. Crosslinking occurs exclusively at open axial metal sites, ensuring that intrinsic node-bound functionalities are retained within the resulting aMOFs.

advantageous properties, including enhanced processability, broad compositional compatibility, tunable optical responses, and, in some cases, improved ion mobility [18–24]. However, only a limited number of bottom-up synthetic strategies have been reported that employ predefined building blocks to rationally introduce functionality into aMOFs [25–29]. These examples rely on direct coordination between metal ions or oxo-clusters and multitopic organic linkers, forming extended amorphous networks through metal-linker crosslinking in a similar manner to the predetermined SBUs of crystalline systems. For instance, zirconium-based aMOFs are synthesized via linker exchange between acetate-capped Zr clusters and ditopic dicarboxylate linkers [28]. Such substitution-based approaches inherently restrict node-level functionalization, as functional groups initially associated with the metal building units are displaced during framework formation, limiting the extent to which functionality can be preprogrammed into the resulting materials.

Here, metal-organic polyhedra (MOPs) are introduced as chemically designable and structurally complex building units to overcome the design limitations of aMOFs. MOPs are discrete, cage-like architectures, some of which feature paddlewheel metal nodes with accessible axial coordination sites, enabling crosslinking to occur without disrupting intrinsic node-bound functionality (Figure 1) [30–36]. Using well-defined rhodium-based MOPs as molecular nodes, extended amorphous frameworks are constructed through post-assembly crosslinking with flexible ditopic linkers. Crucially, this strategy preserves functional groups embedded within the MOP building blocks, allowing molecular-level properties to be directly transferred to the resulting aMOFs. As demonstrated here using a sulfonated Rh-based MOP, crosslinking with bis-pyridinyl and bis-imidazole linkers yields a series of amorphous frameworks in which the MOP units are preserved, as confirmed by pair distribution function analysis. Variations in proton conductivity across the resulting materials, including an aMOF constructed from functional-group-free MOP, highlight the roles of node-bound functional groups, linker flexibility, and the spatial separation of acidic sites, underscoring the potential of MOP-based assembly as a platform for functionally programmable aMOFs.

2 | Results and Discussion

2.1 | Synthesis and Crystal Structure of SO_3RhMOP

The sulfonate-rich metal-organic polyhedral building unit (SO_3RhMOP) was synthesized by reacting rhodium(II) acetate dimer with 5-sulfo-1,3-benzenedicarboxylic acid monosodium salt ($\text{NaSO}_3\text{bdcH}_2$) in a mixed solvent of *N,N*-dimethylacetamide (DMA) and water at 120°C for 24 h (Figure 2A, see detailed methods in the ESI). The resulting purple solution was left to stand at room temperature for one month, during which purple single crystals suitable for single-crystal X-ray diffraction (SCXRD) analysis were obtained (Figure 2B). In this work, SO_3RhMOP was synthesized using the sodium salt $\text{NaSO}_3\text{bdcH}_2$ rather than the protonated ligand isophthalate-5-sulfonic acid ($\text{HSO}_3\text{bdcH}_2$) in order to prevent undesired self-polymerization into crystalline MOF, which potentially occurs when the sulfonic groups are present in their protonated form [37, 38].

SCXRD analysis revealed that SO_3RhMOP crystallizes in the $I4/m$ space group, the same space group as SO_3RhMOP prepared from $\text{HSO}_3\text{bdcH}_2$ [37], with two polyhedral molecules per unit cell (Table S1 and Figure S1). Each discrete molecule is composed of twelve Rh_2 paddlewheel units interconnected by twenty-four sodium 5-sulfo-1,3-benzenedicarboxylate ligands, forming a cuboctahedral architecture (Figure 2C,D). The external axial sites are occupied by DMA and water molecules, whereas internal axial sites of all the Rh_2 paddlewheels are coordinated by dimethylamine (Me_2NH) molecules, which are generated in situ via hydrolysis of DMA under solvothermal reaction conditions. These structural features are essentially the same as SO_3RhMOP prepared from $\text{HSO}_3\text{bdcH}_2$ [37].

Although the positions of Na^+ cations could not be refined crystallographically, their presence was confirmed by inductively coupled plasma-optical emission spectroscopy (ICP-OES), which indicated a $\text{Na}^+:\text{Rh}^{2+}$ ratio to be approximately 0.8:1 (Table S2). Combined results from SCXRD and ICP-OES analyses establish the chemical formula of the polyhedron in its single-crystal form as $\text{H}_{4.8}\text{Na}_{19.2}[\text{Rh}_{24}(\text{SO}_3\text{bdc})_{24}(\text{Me}_2\text{NH})_{12}(\text{H}_2\text{O})_4(\text{DMA})_8]$. Charge neutrality must be achieved by partial protonation of the $-\text{SO}_3^-$

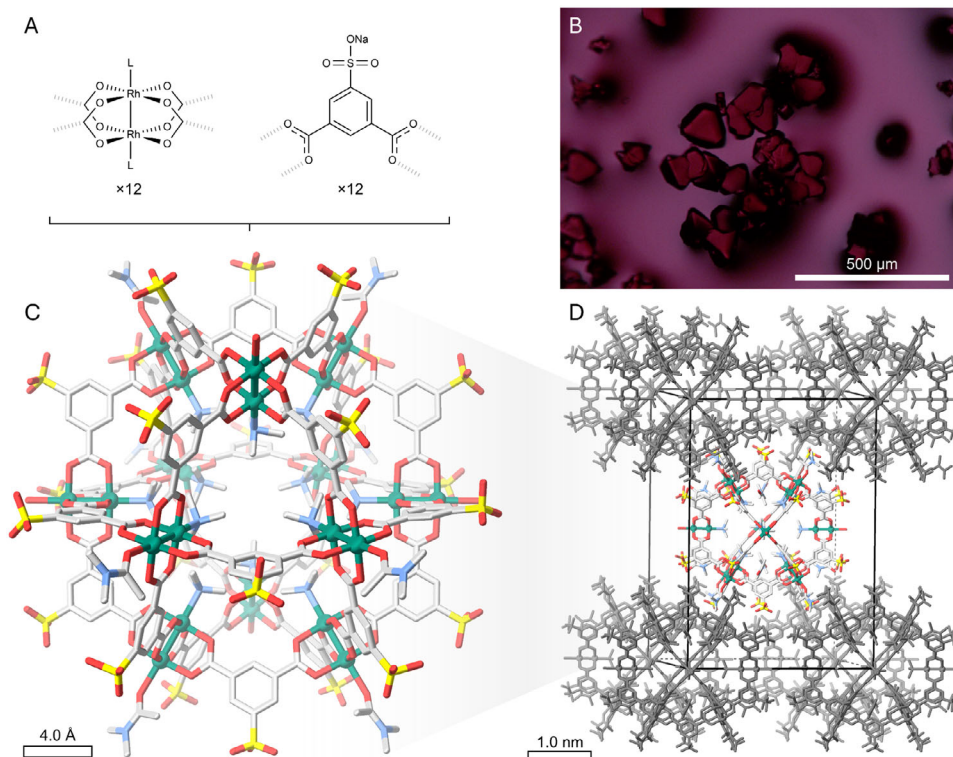


FIGURE 2 | Crystal structure of SO₃RhMOP. (A) The structure of the dirhodium paddlewheel and the sodium 5-sulfo-1,3-benzenedicarboxylate ligands (NaSO₃bdc)²⁻. (B) Optical microscopy image of the as-synthesized SO₃RhMOP in the original solution. (C) The crystal structure and (D) packing structure of SO₃RhMOP. Rh, S, O, C, and N atoms are represented in green, yellow, red, gray, and light blue, respectively. H atoms are omitted for clarity.

[37], where protons are assumed to originate from the hydrolysis of DMA. Compared to previously reported crystal structures of H₂₄[Rh₂₄(SO₃-bdc)₂₄(Me₂NH)₁₂(H₂O)₄(DMA)₈], which contains no Na⁺ cations, the unit cell volume observed in this study is significantly larger. The former has a larger unit cell volume than that of the latter at lower temperature (36919.9(4) Å³ at 170 K versus 35930.3(7) Å³ at 200 K), which is consistent with the incorporation of Na⁺ cations into the structure (Table S1).

We further synthesized SO₃RhMOP powder on a larger scale (see detailed method in ESI). After washing the sample thoroughly with fresh DMA and acetone, subsequent drying at 85°C yielded a purple amorphous powder. The loss of crystallinity was confirmed by powder X-ray diffraction (PXRD, Figure S2). The amorphous nature of SO₃RhMOP in the powder form is attributed to its hygroscopicity and the inherently weak intermolecular interactions between discrete polyhedral units [39]. Notably, the as-synthesized crystals also lose crystallinity upon removal from their mother liquor. Synchrotron pair distribution function (PDF) analysis revealed that the short- to intermediate-range structure of amorphous SO₃RhMOP closely resembles the simulated PDF pattern derived from the single-crystal model (Figures S3, S4). Further discussion of the PDF analysis is provided in a later section. The overall composition of the bulk SO₃RhMOP was characterized by ¹H nuclear magnetic resonance (NMR) spectroscopy (Figures S5, S6) and thermogravimetric analysis (Figure S7 and Table S3).

2.2 | Synthesis of Crosslinked SO₃RhMOP

To construct aMOFs, SO₃RhMOPs were employed as sulfonate-rich molecular building units and crosslinked via ditopic linkers. Rh–Rh paddlewheel clusters in Rh-based MOPs are known to be inert at their equatorial sites but readily exchange coordination bonds at their axial positions, particularly with N-donor linkers [40, 41]. Three flexible ditopic linkers, 1,4-bis[(1*H*-imidazol-1-yl)methyl]benzene (BIX), 1,3-di(4-pyridyl)-propane (DPP), and 1,2-bis(4-pyridyl)ethane (DPE), were selected to promote the formation of amorphous products (Figure 3A).

For the synthesis of aMOFs, SO₃RhMOP and each ditopic linker were first dissolved separately in DMF to afford clear solutions. The SO₃RhMOP-DMF solution was then added to the vigorously stirring linker-DMF solution, producing red solutions containing kinetically trapped species (Figure S8), in which each SO₃RhMOP is coordinated by the ditopic linker in a monodentate fashion [42]. Coordination of the linkers to SO₃RhMOP in DMF was confirmed by the λ_{max} shifts in the UV–vis spectra [33, 41]. The absorption maximum at 551 nm, observed for SO₃RhMOP, shifted to 528, 521, and 521 nm upon addition of 12 molar equivalents of BIX, DPP, and DPE, respectively (Figure S9). Heating the solutions to 120°C for 24 h induced gelation. The gelation indicates that crosslinking between MOP units occurs upon heating, driven by the simultaneous dissociation of excess linkers and the subsequent crosslinking of MOPs by the remaining coordinated linkers (Figure S10) [43, 44]. The resulting gels were washed and

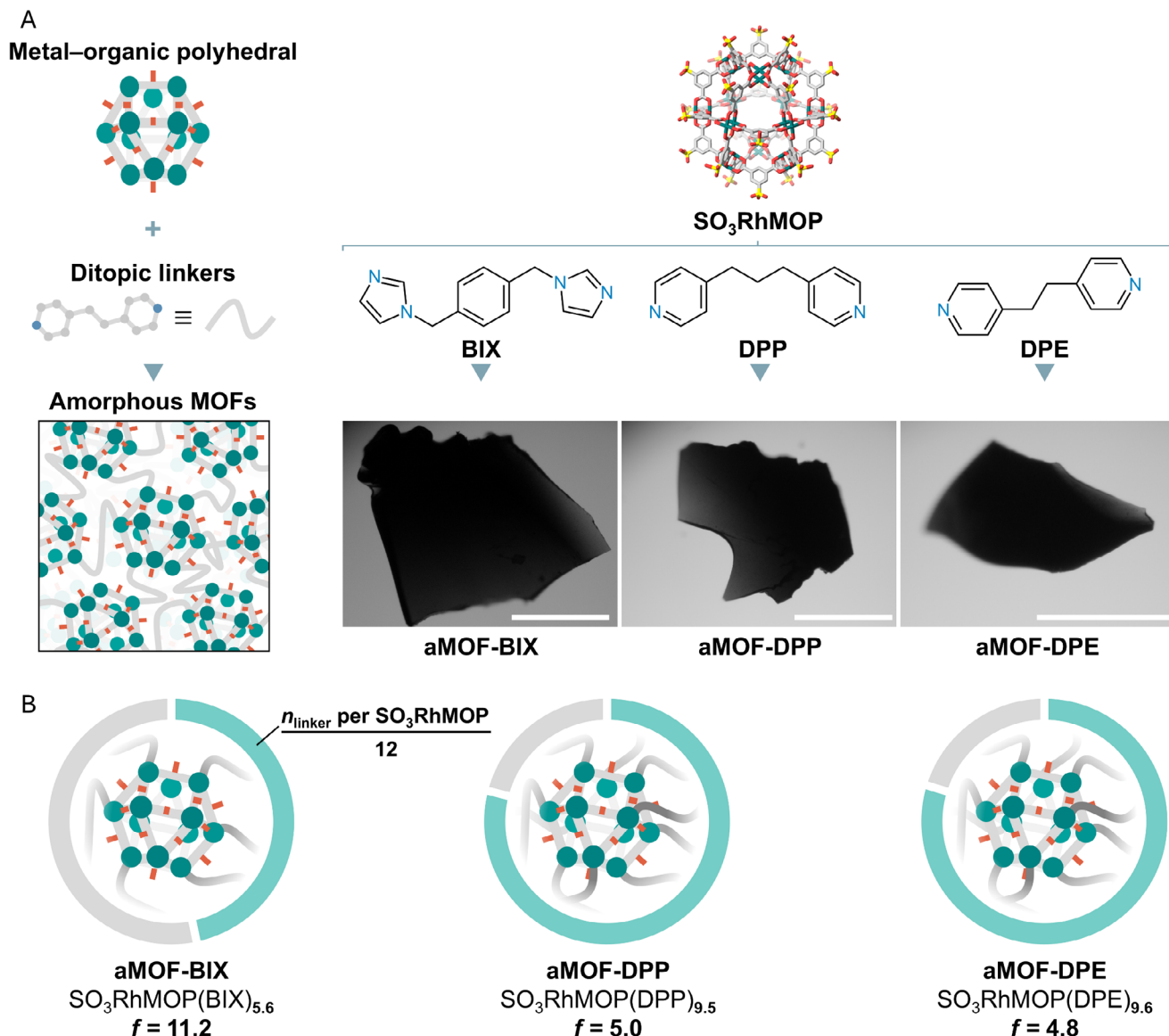


FIGURE 3 | (A) Schematic overview of the bottom-up synthesis of amorphous metal–organic frameworks (aMOFs) using metal–organic polyhedra as building units. Optical images of the resulting aMOF constructed from the ditopic linkers 1,4-bis[(1*H*-imidazol-1-yl)methyl]benzene (BIX), 1,3-di(4-pyridyl)propane (DPP), and 1,2-bis(4-pyridyl)ethane (DPE). Scale bar = 0.5 mm. (B) Donut-chart representation of the number of unique linkers (n_{linker}) coordinated to each SO₃RhMOP node (maximum = 12), derived from the ¹H NMR spectra of the digested aMOFs (Figures S23–S33), along with the corresponding calculated network branch functionality, f . The f value represents the average number of linkers (bridges) emanating from each SO₃RhMOP (junction) in the aMOF, assuming that each ditopic linker preferentially coordinates to two distinct SO₃RhMOPs. Given the 12 exohedral Rh coordination sites per SO₃RhMOP, the theoretical maximum f value is 12, corresponding to full utilization of all sites to connect 12 neighboring SO₃RhMOP via 6 ditopic linkers per SO₃RhMOP (see more detail in ESI Figure S34).

then dried at 80°C for 24 h followed by 120°C for an additional 24 h (see detailed method in ESI), affording dense solids with smooth surfaces at both the macroscopic (Figure 3A) and microscopic (Figures S11–S16) scales. The samples are referred to as aMOF-BIX, aMOF-DPP, and aMOF-DPE, according to the linker employed during crosslinking. The amorphous nature of all samples was confirmed by the broad, diffuse scattering features observed in their PXRD patterns (Figure S17). Thermogravimetric analysis under N₂ showed an initial weight loss of 7.5–8.6 wt% (Figures S18–S21), attributed to dehydration, followed by a plateau indicating that the aMOFs are thermally stable up to at least 225°C. Differential scanning calorimetry (DSC, Figure S22)

measurements of all samples revealed no endothermic baseline shift within the measurement temperature range, indicating the absence of a detectable glass transition temperature and supporting their classification as aMOFs [45].

2.3 | Network Structure of aMOFs

¹H NMR analysis of acid-digested aMOFs reveals that the average numbers of incorporated linkers per polyhedron (n_{linker}) are 5.6, 9.5, and 9.6 for aMOF-BIX, aMOF-DPP, and aMOF-DPE, respectively (Figure 3B; Figures S23–S33). Because each

SO₃RhMOP possesses 12 exohedral Rh sites available for linker coordination, full saturation corresponds to $n_{\text{linker}} = 12$ (Figure S34). Locally, all three aMOFs consist of SO₃RhMOP nodes that function as “junctions,” interconnected by ditopic linkers acting as “bridges” through coordination bonds. The average number of bridges emanating from each junction, and thereby connecting the network, is defined as the network branch functionality, f [46, 47]. Assuming that each ditopic linker preferentially coordinates to two distinct junctions, the f value can be estimated directly from the measured n_{linker} values (Figure 3B; Figure S34).

For aMOF-BIX, the f value is estimated to be 11.2, approaching the theoretical maximum for this system ($f_{\text{max}} = 12$). This indicates that nearly all the exohedral Rh sites participate in bridging interactions with unique SO₃RhMOP neighbors, yielding a highly crosslinked network. The f value observed for aMOF-BIX is notably high relative to previously reported amorphous gels or aerogels constructed from other Rh-based MOPs and BIX linkers. For example, reacting 1-dodecyl-1H-imidazole-stabilized [Rh₂(benzene-1,3-dicarboxylate)₂]₁₂ with BIX produces gels and aerogels with f values between 3.0 and 6.6 [48]. The f value for aMOF-BIX is comparable to the maximum connectivity achieved for [Rh₂(5-dodecoxybenzene-1,3-dicarboxylate)₂]₁₂, for which $f = 12$ was reported under optimized synthesis conditions and depending on the physical form of the product [33, 49].

Both aMOF-DPP and aMOF-DPE exhibit lower f values (5.0 and 4.8, respectively) than aMOF-BIX. This reduction arises because a substantial fraction of the linkers coordinate to the SO₃RhMOP node in a monodentate fashion, thereby decreasing the number of bridging connections per node and consequently lowering the f values [49]. A plausible explanation for the difference between aMOF-BIX and aMOF-DPP/aMOF-DPE lies in the differing basicities of their N-donor sites. During the crosslinking process, BIX, whose conjugate acid has a higher pK_a than those of DPP and DPE, is more readily protonated. For reference, the pK_a values reported for 1-methylimidazole and 4-methylpyridine are 7.20 and 6.02, respectively [50, 51]. Protonation facilitates the temporary generation of additional vacant Rh sites, which can subsequently be occupied by other BIX molecules already coordinated to neighboring SO₃RhMOP nodes. This equilibrium (the site-opening and re-coordination processes mediated by protons) promotes a higher degree of crosslinking in aMOF-BIX, consistent with its larger f value [49, 52].

2.4 | Short-Range Structure

Retention of SO₃RhMOP building units in amorphous aMOF samples was characterized using synchrotron X-ray total scattering combined with PDF analysis (Figure 4A,B) [53]. Fourier transformation of the total structure factor, $S(Q)$, with application of the Lorch modification yields the PDF, $G(r)$, which provides real-space structural information by describing the probability of finding atomic pairs at specific interatomic distances (Figures S35–S41) [54–56]. Assignment of the PDF features was supported by comparison with the simulated PDF pattern and partial PDFs calculated from the single-crystal structure of SO₃RhMOP (Figure S4). The observed PDF peaks can be grouped into four distinct regions, as highlighted in Figure 4A and B. Region I (1.5–2.5 Å) corresponds to interatomic distances within the Rh₂

paddlewheel units. Region II (2.5–7.5 Å) comprises distances between Rh atoms and portions of the coordinated linkers. Region III (7.5–12 Å) covers distances between neighboring Rh₂ paddlewheel units. Region IV (12–24 Å) represents correlations within a single SO₃RhMOP polyhedron [57]. The PDF features of aMOF-BIX, aMOF-DPP, and aMOF-DPE closely resemble those of SO₃RhMOP, including retention of the Rh...Rh₄ correlations at interatomic distances of approximately 16–17 Å. Together with the comparable Fourier transform infrared (FTIR, Figure S42) spectra observed for SO₃RhMOP and the corresponding aMOFs, these results confirm that the SO₃RhMOP building units remain intact in all aMOFs [28]. This behavior contrasts with zeolitic imidazolate framework glasses, where the melt-quenching process induces short-range disorder arising from distortions of the Zn[ligand]₄ tetrahedral units [58]. At higher r values, the PDFs become largely featureless due to signal damping originating from the amorphous nature of the samples [59].

2.5 | Free Volume of aMOFs

Changes in the average pore radius and free volume between SO₃RhMOP and the corresponding aMOFs with different linker identities under ambient conditions, without sample activation, were monitored using positron annihilation lifetime spectroscopy (PALS, Figure 5; Figure S43). The orthopositronium (*o*-Ps) lifetime (τ_3) and its relative intensity (I_3), corresponding to the longest-lived component, are correlated with the average pore radius and the relative number of free-volume cavities, respectively [60]. The estimated pore radii (and corresponding τ_3 values) for SO₃RhMOP, aMOF-BIX, aMOF-DPP, and aMOF-DPE are 0.282 nm (1.96 ns), 0.290 nm (2.04 ns), 0.271 nm (1.84 ns), and 0.275 nm (1.89 ns), respectively. The PALS-derived free-volume parameters ($\tau_3^3 I_3$) are 20.7, 18.9, 14.1, and 15.5 ns³%, respectively. Among the aMOF samples, these trends are consistent with the N₂ gas-accessible porosity data, indicating that the free volume is strongly influenced by linker rigidity (see detail in ESI, Figure S44). Considering that all samples are predominantly composed of SO₃RhMOP units, the comparatively higher free-volume parameter observed for pristine SO₃RhMOP likely originates from external cavities formed by loosely packed SO₃RhMOP units and incorporated interstitial water molecules [37, 61].

2.6 | Water Stability and Proton Conductivity

The presence of a high density of hydrophilic moieties in SO₃RhMOP and the corresponding aMOFs, including sulfonate groups and Na⁺ ions, motivated us to evaluate their proton conductivity [62, 63]. Previous studies have shown that MOPs containing sulfonic acid groups exhibit promising proton conductivities, reaching approximately 15 mS cm^{−1} at 85°C and 90% relative humidity (RH), and up to 25 mS cm^{−1} at 95°C [37]. Although high proton conductivity can be achieved with discrete MOPs, their practical application is limited by their high water solubility, which leads to a significant risk of dissolution upon exposure to liquid water during condensation events [64].

Water stability was therefore assessed by immersing all materials in deionized water at 25°C under static conditions for two months (Figure S45). SO₃RhMOP remained solid without undergoing

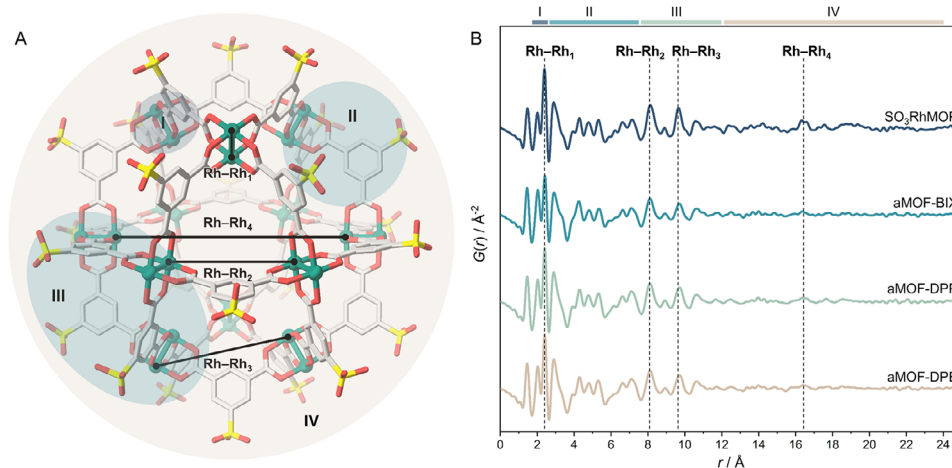


FIGURE 4 | (A) Local coordination environment and pair-distance labeling in SO_3RhMOP . Rh, S, O, and C atoms are represented in green, yellow, red, and gray, respectively. H atoms and solvent molecules are omitted for clarity. (B) Experimental pair distribution functions (PDFs) of SO_3RhMOP , aMOF-BIX, aMOF-DPP, and aMOF-DPE. Peaks are grouped into four main regions, highlighted in (A). Peak labels are assigned based on partial PDFs (Figure S4) simulated from crystal structures of SO_3RhMOP . Additional $S(Q)$ data and extended PDF data up to 40 Å are provided in Figures S35–S41 of the ESI.

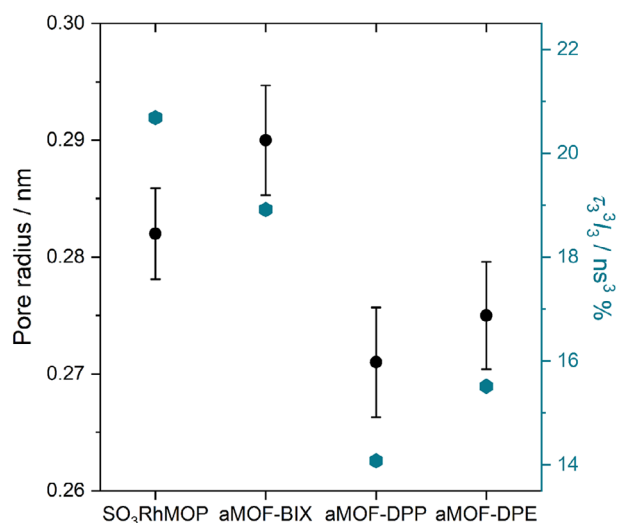


FIGURE 5 | Pore radius of SO_3RhMOP , aMOF-BIX, aMOF-DPP, aMOF-DPE, and PALS parameter ($\tau_3^3 I_3$). These cavity sizes were derived from the orthopositronium (*o*-Ps) lifetime component (τ_3) obtained via Positron Annihilation Lifetime Spectroscopy (PALS). See Figure S43 for the PALS spectra and Table S4 for the complete parameters.

deliquescence at 90% RH and 85°C. However, upon direct contact with liquid water, it dissolved immediately and was completely dissolved within 2 h. Similarly, aMOF-DPP exhibited substantial dissolution and fully dissolved after 7 days. In contrast, no visually detectable dissolution was observed for aMOF-BIX or aMOF-DPE over the two-month period. The water stability of aMOF-BIX and aMOF-DPE was further evaluated at elevated temperature by immersing the samples in water at 70°C for 24 h (Figure S46). Under these conditions, aMOF-DPE completely dissolved, indicating that the apparent water stability observed at room temperature is kinetically limited. In contrast, aMOF-BIX remained stable, with no detectable dissolution observed by UV–

vis spectroscopy (Figure S47). This difference in water stability correlates well with the pK_a values of the linkers employed.

Based on their water stability at room temperature, aMOF-BIX and aMOF-DPE were selected for further proton conductivity evaluation under humidified conditions, in comparison with pristine SO_3RhMOP (Figure 6A). All samples were prepared as pressed pellets from powder, and their proton conductivities were measured using alternating-current (AC) impedance spectroscopy under a humidified atmosphere at 90% RH. Pristine SO_3RhMOP exhibits a proton conductivity of 2.0 mS cm^{-1} at 30°C, which increases to 16.7 mS cm^{-1} as the temperature is raised to 85°C. The activation energy (E_a) for proton conduction was determined to be 0.40 eV, which lies at the empirical boundary commonly used to distinguish between the Grotthuss and vehicle mechanisms [65–67, 13]. Notably, negligible conductivity was observed at 100°C under dry N_2 atmosphere, indicating that charge transport is predominantly mediated by incorporated water [68]. Proton migration is therefore likely to proceed via hopping through a hydrogen-bonding network composed primarily of water molecules, stabilized by interactions with hydrophilic sulfonate groups and hydrated Na^+ ions [69].

Crosslinking the proton-conductive moiety (in this case SO_3RhMOP) typically decreases conductivity dramatically, often due to an increase in spatial separation and a decrease in the degree of freedom in motion caused by crosslinking [70]. However, aMOF-DPE exhibits conductivity of 1.6 mS cm^{-1} at 30°C, comparable to that of SO_3RhMOP at 30°C (Figure 6A). We attribute this suppression of the negative impact of crosslinking to the relatively small spatial separation of aMOF-DPE (Figure 5). In addition, the presence of non-coordinated pyridyl groups on the monodentate DPE linker, as suggested by the smaller f value of aMOF-DPE, may provide additional hopping sites that facilitate proton migration. The proton conductivity of aMOF-DPE reaches 4.8 mS cm^{-1} at 85°C with an E_a of 0.20 eV. The benefit of crosslinking (enhanced water stability) is remarkable in aMOF-DPE, considering the limited drop of conductivity

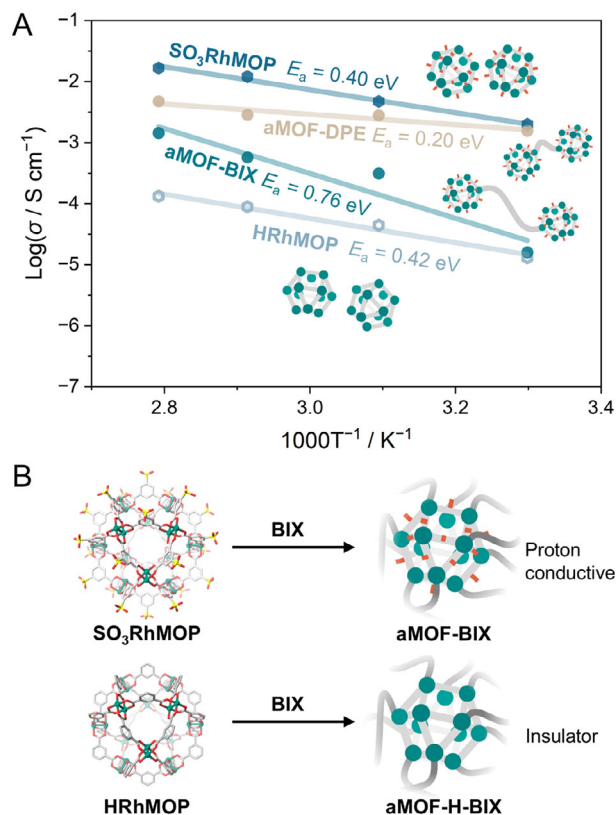


FIGURE 6 | (A) Variable temperature proton conductivity at 90% relative humidity (RH) of SO_3RhMOP , aMOF-BIX, aMOF-DPE, and HRhMOP. Nyquist plots are provided in Figures S48–S54. The activation energy (E_a) values were calculated from Arrhenius plots (Figure S55). Conductivity values are provided in Table S9. (B) Schematic illustration of the contributions of node-bound functional groups to humidity-dependent proton conductivity. Rh, S, O, and C atoms are represented in green, yellow, red, and gray, respectively. H atoms and solvent molecules are omitted for clarity.

and lowered E_a compared to those of SO_3RhMOP . Notably, aMOF-DPE retains its fine powder morphology without any observable swelling after 8 h under humidified conditions (90% RH and 85°C, Figure S57).

The drop in conductivity is more prominent in aMOF-BIX. aMOF-BIX exhibits a proton conductivity of 0.016 mS cm^{-1} at 30°C, increasing to 1.4 mS cm^{-1} at 85°C with E_a of 0.76 eV (Figure 6A). The substantial decrease in proton conductivity, accompanied by an increase in E_a relative to SO_3RhMOP , is potentially attributed to the larger spatial separation between sulfonate groups (Figure 5) and the restricted mobility imposed by the relatively rigid BIX linker and the highly crosslinked network ($f = 11.2$). In addition, aMOF-BIX shows lower water uptake compared to aMOF-DPE. For example, aMOF-BIX contains 26.3wt% H_2O , which is lower than the 32.2 wt% observed for aMOF-DPE under identical conditions (30°C and 90% RH, Figure S58). The higher hydration level in aMOF-DPE is expected to facilitate proton transport under humidified conditions [71]. Nonetheless, the conductivity of aMOF-BIX is comparably high to the best value of the previously reported Zr-based aMOFs synthesized via bottom-up approaches, where water-mediated proton conductivity is governed predominantly by the acidity of

functional groups on the organic linkers (0.031 mS cm^{-1} at 30°C and 95% RH) [28]. The superior performance of aMOF-DPE and aMOF-BIX suggests the advantage of the material design using the node-bound functionality.

The importance of node-bound functionality is further highlighted by an analogous aMOF without a functional group. We prepared this aMOF (hereafter aMOF-H-BIX) from a sulfonate-free MOP [72], $[\text{Rh}_{24}(\text{Hbdc})_{24}]$ (hereafter HRhMOP) and the ditopic BIX linker (see ESI Figures S59–S66 for detailed synthesis and characterization). Notably, the proton conductivity of aMOF-H-BIX ($f = 5.5$, see ESI) was below the instrumental limit, effectively making it an insulator (Figure 6B; Figure S67). The proton conductivity of discrete HRhMOP at 90% RH exhibited values of 0.013 and 0.13 mS cm^{-1} at 30 and 85°C, respectively, which is lower than the values of aMOF-DPE and aMOF-BIX throughout the measured temperature range. The observed difference in conductivity demonstrates the effectiveness of our bottom-up strategy, where we can preserve functional groups embedded within the MOP building blocks.

Millimeter-scale, self-standing aMOF-BIX films can be fabricated by reducing the thickness of the kinetically trapped solution within an enclosed container during gelation without modifying other synthesis parameters. This approach reduces the thickness of the resulting cross-linked gel and, consequently, the final aMOF material after drying. For example, maintaining a solution height of 4 mm yields aMOF-BIX films with a thickness of approximately $11 \mu\text{m}$ (Figure S68). In contrast, aMOF-DPE is more difficult to process into large-area films (Figure S69), likely due to its lower degree of cross-linking. Nevertheless, these results indicate that film formation is feasible through geometric control of the reaction medium. With further optimization of synthesis conditions, particularly solution thickness and drying protocols, the fabrication of application-ready, self-standing aMOF films is achievable.

3 | Conclusions

In conclusion, we have demonstrated a bottom-up approach to amorphous metal–organic frameworks that decouples network formation from node functionalization by employing sulfonate-rich metal–organic polyhedra as molecular building units. This strategy enables the preservation of well-defined Rh-based MOP architectures within extended amorphous networks while allowing modulation of network connectivity, free volume, and transport properties through the choice of linkers. The resulting aMOFs exhibit enhanced water stability relative to the discrete MOP precursor and display tunable proton conductivity governed by linker flexibility, sulfonate spatial arrangement, and water-mediated transport pathways. The aMOFs constructed from sulfonated Rh-based MOPs exhibit proton conductivities exceeding those of previously reported aMOFs from the bottom-up approach, whereas aMOFs synthesized from functional-group-free MOPs display insulating behavior. These results underscore the important role of node-level functionality in amorphous framework design. Additionally, dual-mode functionality can be developed to enhance proton conductivity by introducing functional groups in both the crosslinkers and the nodes. More broadly, this work establishes MOP-based assembly as a

versatile and general paradigm for the rational construction of functionally programmable aMOFs, opening new avenues for the design of disordered solids with precisely encoded molecular properties.

Acknowledgements

N.M. acknowledges the support from ICYS for a research fellowship, from the Japan Science and Technology Agency (JST) PRESTO grant JPMJPR25MB, from the Japan Society of the Promotion of Science (JSPS) KAKENHI Grant Numbers JP24K23109 and JP25K18055, from the Sumitomo Foundation basic science grant number 2402150, and from the Iketani Science and Technology Foundation grant number 0371207-A. S.K. acknowledges the support from ICYS for a research fellowship and from JST NEXUS (JPMJNX25B4). The authors acknowledge the BL04B2 beamlines at SPring-8 for the synchrotron X-ray total scattering experiments with the approval of JASRI (Proposal Numbers 2024B1167, 2025A1067, and 2025B1248). The authors thank Dr. Takashi Nakanishi (NIMS), Dr. Renzhi Ma (NIMS), and Dr. Michio Matsumoto (NIMS) for providing access to equipment. The authors acknowledge support from the NIMS Surface and Bulk Analysis Unit and NIMS Nanofabrication Facilities. N. M. acknowledges the discussions with Dr. Takashi Nakanishi (NIMS), Dr. Michio Matsumoto (NIMS), Dr. Shinsuke Ishihara (NIMS), Dr. Mizuki Tenjimbayashi (NIMS), Dr. Kazuhiko Nagura (NIMS), and Prof. Rob Ameloot (KU Leuven). Finally, N. M. acknowledges the support from Dr. Koichi Tsuchiya, Ms. Chikako Enari, Ms. Imanishi Yuko, and Mr. Kenichiro Kono.

Conflicts of Interest

The authors declare no conflict of interest.

Data Availability Statement

Deposition number 2529690 (for SO_3RhMOP) contains the supplementary crystallographic data for this paper. These data are provided free of charge by the joint Cambridge Crystallographic Data Centre and Fachinformationszentrum Karlsruhe Access Structures service.

References

1. B. F. Hoskins and R. Robson, "Infinite Polymeric Frameworks Consisting of Three Dimensionally Linked Rod-Like Segments," *Journal of the American Chemical Society* 111 (1989): 5962–5964, <https://doi.org/10.1021/ja00197a079>.
2. M. Kondo, T. Yoshitomi, H. Matsuzaka, S. Kitagawa, and K. Seki, "[$\text{M}_2(4, 4'\text{-bpy})_3(\text{NO}_3)_4 \cdot x\text{H}_2\text{O}$] $_n$ ($\text{M} = \text{Co}, \text{Ni}, \text{Zn}$)," *Angewandte Chemie International Edition* 36 (1997): 1725–1727.
3. H. Li, M. Eddaoudi, T. L. Groy, and O. M. Yaghi, "Establishing Microporosity in Open Metal–Organic Frameworks: Gas Sorption Isotherms for $\text{Zn}(\text{BDC})$ ($\text{BDC} = 1,4\text{-Benzenedicarboxylate}$)," *Journal of the American Chemical Society* 120 (1998): 8571–8572.
4. M. Eddaoudi, J. Kim, and N. Rosi, "Systematic Design of Pore Size and Functionality in Isorecticular MOFs and Their Application in Methane Storage," *Science* 295 (2002): 469–472, <https://doi.org/10.1126/science.1067208>.
5. O. M. Yaghi, M. O'Keeffe, N. W. Ockwig, H. K. Chae, M. Eddaoudi, and J. Kim, "Reticular Synthesis and the Design of New Materials," *Nature* 423 (2003): 705–714, <https://doi.org/10.1038/nature01650>.
6. C. Serre, F. Millange, S. Surblé, and G. Férey, "A Route to the Synthesis of Trivalent Transition-Metal Porous Carboxylates With Trimeric

Secondary Building Units," *Angewandte Chemie International Edition* 43 (2004): 6285–6289, <https://doi.org/10.1002/anie.200454250>.

7. S. Kitagawa, R. Kitaura, and S. Noro, "Functional Porous Coordination Polymers," *Angewandte Chemie International Edition* 43 (2004): 2334–2375, <https://doi.org/10.1002/anie.200300610>.
8. G. Férey, "Hybrid Porous Solids: Past, Present, Future," *Chemical Society Reviews* 37 (2008): 191–214.
9. L. J. Murray, M. Dincă, and J. R. Long, "Hydrogen Storage in Metal–organic Frameworks," *Chemical Society Reviews* 38 (2009): 1294–1314.
10. J. Lee, O. K. Farha, J. Roberts, K. A. Scheidt, S. T. Nguyen, and J. T. Hupp, "Metal–organic Framework Materials as Catalysts," *Chemical Society Reviews* 38 (2009): 1450–1459.
11. Y.-S. Wei, M. Zhang, R. Zou, and Q. Xu, "Metal–Organic Framework-Based Catalysts With Single Metal Sites," *Chemical Society Reviews* 120 (2020): 12089–12174.
12. P. Ramaswamy, N. E. Wong, and G. K. H. Shimizu, "MOFs as Proton Conductors – challenges and Opportunities," *Chemical Society Reviews* 43 (2014): 5913–5932.
13. D.-W. Lim and H. Kitagawa, "Proton Transport in Metal–Organic Frameworks," *Chemical Review* 120 (2020): 8416–8467.
14. L. S. Xie, G. Skorupskii, and M. Dinca, "Electrically Conductive Metal–Organic Frameworks," *Chemical Reviews* 120 (2020): 8536–8580, <https://doi.org/10.1021/acs.chemrev.9b00766>.
15. G. M. Espallargas and E. Coronado, "Magnetic Functionalities in MOFs: From the Framework to the Pore," *Chemical Society Reviews* 47 (2018): 533–557, <https://doi.org/10.1039/C7CS00653E>.
16. A. E. Thorarindottir and T. D. Harris, "Metal–Organic Framework Magnets," *Chemical Review* 120 (2020): 8716–8789.
17. T. D. Bennett and S. Horike, "Liquid, Glass and Amorphous Solid States of Coordination Polymers and Metal–organic Frameworks," *Nature Reviews Materials* 3 (2018): 431–440, <https://doi.org/10.1038/s41578-018-0054-3>.
18. W. Chen, S. Horike, and D. Umeyama, "Glass Formation of a Coordination Polymer Crystal for Enhanced Proton Conductivity and Material Flexibility," *Angewandte Chemie International Edition* 55 (2016): 5195–5200, <https://doi.org/10.1002/anie.201600123>.
19. L. Frentzel-Beyme, M. Klotz, P. Kolodzeiski, R. Pallach, and S. Henke, "From Melting Point Engineering to Selective Hydrocarbon Sorption," *Journal of the American Chemical Society* 141 (2019): 12362–12371, <https://doi.org/10.1021/jacs.9b05558>.
20. Y. Wang, H. Jin, and Q. Ma, "A MOF Glass Membrane for Gas Separation," *Angewandte Chemie International Edition* 59 (2020): 4365–4369, <https://doi.org/10.1002/anie.201915807>.
21. M. Liu, A. H. Slavney, and S. Tao, "Designing Glass and Crystalline Phases of Metal–Bis(acetamide) Networks to Promote High Optical Contrast," *Journal of the American Chemical Society* 144 (2022): 22262–22271.
22. N. Ma, S. Impeng, S. Bureekaew, N. Morozumi, M. Haga, and S. Horike, "Photoexcited Anhydrous Proton Conductivity in Coordination Polymer Glass," *Journal of the American Chemical Society* 145 (2023): 9808–9814, <https://doi.org/10.1021/jacs.3c01821>.
23. M. Kim, H.-S. Lee, D.-H. Seo, S. J. Cho, E. Jeon, and H. R. Moon, "Melt-quenched Carboxylate Metal–organic Framework Glasses," *Nature Communications* 15 (2024): 1174.
24. F. Cao, S. S. Sørensen, and A. K. R. Christensen, "Continuous Structure Modification of Metal–organic Framework Glasses via Halide Salts," *Nature Communications* 16 (2025): 7001, <https://doi.org/10.1038/s41467-025-62143-9>.
25. T. Ogawa, K. Takahashi, and S. S. Nagarkar, "Coordination Polymer Glass from a Protic Ionic Liquid: Proton Conductivity and Mechanical

- Properties as an Electrolyte,” *Chemical Science* 11 (2020): 5175–5181, <https://doi.org/10.1039/D0SC01737J>.
26. T. Ogawa, K. Takahashi, and T. Kurihara, “Network Size Control in Coordination Polymer Glasses and Its Impact on Viscosity and H⁺ Conductivity,” *Chemistry of Materials* 34 (2022): 5832–5841.
27. Z. Zhang and Y. Zhao, “Transparent and High-porosity Aluminum Alkoxide Network-forming Glasses,” *Nature Communications* 15 (2024): 7339, <https://doi.org/10.1038/s41467-024-51845-1>.
28. N. Ma, S. Kosasang, and J. Theissen, “Systematic Design and Functionalisation of Amorphous Zirconium Metal–organic Frameworks,” *Chemical Science* 15 (2024): 17562–17570.
29. L. León-Alcaide, L. Martínez-Goyeneche, and M. Sessolo, “Direct Synthesis of an Iron Metal–organic Framework Antiferromagnetic Glass,” *Nature Communications* 16 (2025): 8783, <https://doi.org/10.1038/s41467-025-63837-w>.
30. J.-R. Li, D. J. Timmons, and H.-C. Zhou, “Interconversion Between Molecular Polyhedra and Metal–Organic Frameworks,” *Journal of the American Chemical Society* 131 (2009): 6368–6369.
31. H.-N. Wang, X. Meng, and G.-S. Yang, “Stepwise Assembly of Metal–organic Framework Based on a Metal–organic Polyhedron Precursor for Drug Delivery,” *Chemical Communications* 47 (2011): 7128–7130.
32. H.-N. Wang, F.-H. Liu, X.-L. Wang, K.-Z. Shao, and Z.-M. Su, “Three Neutral Metal–organic Frameworks With Micro- and Meso-pores for Adsorption and Separation of Dyes,” *Journal of Materials Chemistry A* 1 (2013): 13060–13063.
33. A. Carné-Sánchez, G. A. Craig, and P. Larpen, “Self-assembly of Metal–organic Polyhedra Into Supramolecular Polymers With Intrinsic Microporosity,” *Nature Communication* 9 (2018): 2506.
34. Z. Wang, C. Villa Santos, and A. Legrand, “Multiscale Structural Control of Linked Metal–organic Polyhedra Gel by Aging-induced Linkage-reorganization,” *Chemical Science* 12 (2021): 12556–12563.
35. T. Grancha, A. Carné-Sánchez, and F. Zarekarizi, “Synthesis of Polycarboxylate Rhodium(II) Metal–Organic Polyhedra (MOPs) and Their Use as Building Blocks for Highly Connected Metal–Organic Frameworks (MOFs),” *Angewandte Chemie International Edition* 60 (2021): 5729–5733.
36. A. Khobotov-Bakishev, L. Hernández-López, C. von Baekmann, J. Albalad, A. Carné-Sánchez, and D. Maspoch, “Metal–Organic Polyhedra as Building Blocks for Porous Extended Networks,” *Advanced Science* 9 (2022): 2104753.
37. J. Troyano, S. Horike, and S. Furukawa, “Reversible Discrete-to-Extended Metal–Organic Polyhedra Transformation by Sulfonic Acid Surface Functionalization,” *Journal of the American Chemical Society* 144 (2022): 19475–19484.
38. B. L. Ouay, T. Ohara, R. Minami, R. Kunitomo, R. Ohtani, and M. Ohba, “Efficient water-based purification of metal–organic polyhedra by centrifugal ultrafiltration,” *Dalton Transactions* 52 (2023): 15321–15325, <https://doi.org/10.1039/D3DT01644G>.
39. S. Tokuda and S. Furukawa, “Three-dimensional van der Waals Open Frameworks,” *Nature Chemistry* 17 (2025): 672–678, <https://doi.org/10.1038/s41557-025-01777-0>.
40. E. Warzecha, T. C. Berto, and J. F. Berry, “Structural and Spectroscopic Study,” *Inorganic Chemistry* 54 (2015): 8817–8824.
41. A. Carné-Sánchez, J. Albalad, and T. Grancha, “Postsynthetic Covalent and Coordination Functionalization of Rhodium(II)-Based Metal–Organic Polyhedra,” *Journal of the American Chemical Society* 141 (2019): 4094–4102.
42. Z. Wang, T. Aoyama, E. Sánchez-González, T. Inose, K. Urayama, and S. Furukawa, “Control of Extrinsic Porosities in Linked Metal–Organic Polyhedra Gels by Imparting Coordination-Driven Self-Assembly With Electrostatic Repulsion,” *ACS Applied Materials & Interfaces* 14 (2022): 23660–23668.
43. D. Nam, J. Huh, and J. Lee, “Cross-linking Zr-based Metal–organic Polyhedra via Postsynthetic Polymerization,” *Chemical Science* 8 (2017): 7765–7771.
44. A. Legrand, G. A. Craig, M. Bonneau, S. Minami, K. Urayama, and S. Furukawa, “Understanding the Multiscale Self-assembly of Metal–organic Polyhedra towards Functionally Graded Porous Gels,” *Chemical Science* 10 (2019): 10833–10842.
45. A. Qiao, T. D. Bennett, and H. Tao, “A Metal–organic Framework With Ultrahigh Glass-forming Ability,” *Science Advances* 4 (2018): aao6827, <https://doi.org/10.1126/sciadv.aao6827>.
46. A. V. Zhukhovitskiy, M. Zhong, and E. G. Keeler, “Highly Branched and Loop-rich Gels via Formation of Metal–organic Cages Linked by Polymers,” *Nature Chemistry* 8 (2016): 33–41.
47. Y. Gu, J. Zhao, and J. A. Johnson, “From Plastics and Gels to Porous Frameworks,” *Angewandte Chemie International Edition* 59 (2020): 5022–5049, <https://doi.org/10.1002/anie.201902900>.
48. Z. Wang, C. Villa Santos, and A. Legrand, “Multiscale Structural Control of Linked Metal–organic Polyhedra Gel by Aging-induced Linkage-reorganization,” *Chemical Science* 12 (2021): 12556–12563.
49. A. Legrand, L.-H. Liu, and P. Royla, “Spatiotemporal Control of Supramolecular Polymerization and Gelation of Metal–Organic Polyhedra,” *Journal of the American Chemical Society* 143 (2021): 3562–3570.
50. H. C. Brown, D. H. McDaniel, and O. Häfliger, in *Determination of Organic Structures by Physical Methods* Ed. E. A. Braude and F. C. Nachod (Academic Press, 1955), 567–662.
51. R. L. Benoit, D. Boulet, L. Séguin, and M. Fréchette, “Protonation of Purines and Related Compounds in Dimethylsulfoxide and Water,” *Canadian Journal of Chemistry* 63 (1985): 1228–1232, <https://doi.org/10.1139/v85-209>.
52. R. S. Forgan, “Modulated Self-assembly of Metal–organic Frameworks,” *Chemical Science* 11 (2020): 4546–4562.
53. H. Yamada, S. Shimono, and S. Kawaguchi, “High-throughput X-ray Total Scattering Measurement System at BL04B2 of SPring-8,” *Journal of Synchrotron Radiation* 33 (2026): 516–522, <https://doi.org/10.1107/S1600577525011294>.
54. T. E. Faber and J. M. Ziman, “A Theory of the Electrical Properties of Liquid Metals,” *Philosophical Magazine* 11 (1965): 153–173, <https://doi.org/10.1080/14786436508211931>.
55. E. Lorch, “Neutron Diffraction by Germania, Silica and Radiation-damaged Silica Glasses,” *Journal of Physics C: Solid State Physics* 2 (1969): 229–237, <https://doi.org/10.1088/0022-3719/2/2/305>.
56. S. Kohara, M. Itou, and K. Suzuya, “Structural Studies of Disordered Materials Using High-energy X-ray Diffraction From Ambient to Extreme Conditions,” *Journal of Physics: Condensed Matter* 19 (2007): 506101, <https://doi.org/10.1088/0953-8984/19/50/506101>.
57. A. C. Ghosh, A. Legrand, and R. Rajapaksha, “Rhodium-Based Metal–Organic Polyhedra Assemblies for Selective CO₂ Photoreduction,” *Journal of the American Chemical Society* 144 (2022): 3626–3636.
58. R. S. K. Madsen, A. Qiao, and J. Sen, “Ultrahigh-field ⁶⁷Zn NMR Reveals Short-range Disorder in Zeolitic Imidazolate Framework Glasses,” *Science* 367 (2020): 1473–1476, <https://doi.org/10.1126/science.aaz0251>.
59. M. W. Terban and S. J. L. Billinge, “Structural Analysis of Molecular Materials Using the Pair Distribution Function,” *Chemical Reviews* 122 (2022): 1208–1272, <https://doi.org/10.1021/acs.chemrev.1c00237>.
60. S. J. Tao, “Positronium Annihilation in Molecular Substances,” *The Journal of Chemical Physics* 56 (1972): 5499–5510, <https://doi.org/10.1063/1.1677067>.
61. L. O. Alimi, N. Khalfay, S. Khelifi, W. Lin, B. Moosa, and N. M. Khashab, “A Nonporous Crystalline Organic Cage for Selective Water Uptake and Storage,” *Chemical Science* 17 (2026): 511–515, <https://doi.org/10.1039/D5SC06328K>.

62. R. Liu, D.-Y. Wang, J.-R. Shi, and G. Li, "Proton Conductive Metal Sulfonate Frameworks," *Coordination Chemistry Reviews* 431 (2021): 213747, <https://doi.org/10.1016/j.ccr.2020.213747>.
63. S.-S. Liu, Q.-Q. Liu, S.-Z. Huang, C. Zhang, X.-Y. Dong, and S.-Q. Zang, "Sulfonic and Phosphonic Porous Solids as Proton Conductors," *Coordination Chemistry Reviews* 451 (2022): 214241, <https://doi.org/10.1016/j.ccr.2021.214241>.
64. K. Takahashi, T. Ogawa, T. Itakura, K. Kami, and S. Horike, "Water-Stable Al(III) Coordination Polymer Glass With High Proton Conductivity Toward Stable Electrolytes in a Fuel Cell," *ACS Applied Energy Materials* 7 (2024): 11937–11945.
65. K.-D. Kreuer, A. Rabenau, and W. Weppner, "Vehicle Mechanism, A New Model for the Interpretation of the Conductivity of Fast Proton Conductors," *Angewandte Chemie International Edition in English* 21 (1982): 208–209, <https://doi.org/10.1002/anie.198202082>.
66. N. Agmon, "The Grotthuss Mechanism," *Chemical Physics Letters* 244 (1995): 456–462, [https://doi.org/10.1016/0009-2614\(95\)00905-J](https://doi.org/10.1016/0009-2614(95)00905-J).
67. T. Ogawa, K. Kamiguchi, T. Tamaki, H. Imai, and T. Yamaguchi, "Differentiating Grotthuss Proton Conduction Mechanisms by Nuclear Magnetic Resonance Spectroscopic Analysis of Frozen Samples," *Analytical Chemistry* 86 (2014): 9362–9366, <https://doi.org/10.1021/ac5021485>.
68. T. Norby, "Solid-state Protonic Conductors: Principles, Properties, Progress and Prospects," *Solid State Ionics* 125 (1999): 1–11.
69. K. D. Kreuer, "Phenomenon Between the Solid and the Liquid state?," *Solid State Ionics* 94 (1997): 55–62, [https://doi.org/10.1016/S0167-2738\(96\)00608-X](https://doi.org/10.1016/S0167-2738(96)00608-X).
70. M. K. Sarango-Ramírez, J. Park, J. Kim, Y. Yoshida, D.-W. Lim, and H. Kitagawa, "Void Space versus Surface Functionalization for Proton Conduction in Metal–Organic Frameworks," *Angewandte Chemie International Edition* 60 (2021): 20173–20177.
71. K. Shiraishi, M. Kabaya, K. Fujihira, K. Kato, and M. Sadakiyo, "A detailed study on the effects of adsorbed water molecules on proton conduction in a metal–organic framework," *Dalton Transactions* 54 (2025): 12125–12129, <https://doi.org/10.1039/D5DT01395J>.
72. S. Furukawa, N. Horike, and M. Kondo, "Rhodium–Organic Cuboctahedra as Porous Solids With Strong Binding Sites," *Inorganic Chemistry* 55 (2016): 10843–10846.

Supporting Information

Additional supporting information can be found online in the Supporting Information section.

Supporting File: sml173752-sup-0001-SuppMat.pdf.